ADVANCED SUSTAINABLE SYSTEMS
www.advsustainsys.com

Magnetic Supramolecular Hydrogel in Situ Polymerization with Acrylated β-Cyclodextrin for the Efficient Adsorption of Pollutants

Wen-Jin An, Xiao-Yong Yu, Chu-Han Liu, Yuan-Li Leng, Yong Chen, and Yu Liu**

Supramolecular hydrogels have significant research implications for the environmental application of dyes and bisphenols wastewater. Herein, a magnetic Fe_3O_4-P(AAm-AMPS-CDA) supramolecular hydrogel is reported, which is constructed by acrylamide, 2-acrylamido-2-methylpropane sulfonic acid, acrylated β-cyclodextrin, and Fe_3O_4 nanoparticles via thermal polymerization, exhibiting good adsorption properties for cationic dyes and bisphenols. UV–vis spectra show that the adsorption efficiencies of the hydrogel reach 96% for crystal violet and 98% for methylene blue. Meanwhile, β-CDA cavities can form an inclusion complex with bisphenols, achieving adsorption efficiencies of 88% for bisphenol A and 69% for bisphenol F, with no significant decrease in adsorption rates even after seven cycles. The adsorption kinetic experiments indicate that the adsorption process follows the pseudo-second-order kinetics model, and the Weber-Morris intraparticle diffusion model reveals the diffusion mechanism. Additionally, in the presence of NaCl and humic acid, the hydrogel still maintains a high adsorption rate, and there is no significant decline in adsorption across different environmental water qualities, indicating that the hydrogel has great application potential. Importantly, the hydrogel exhibits ferromagnetic characteristics, allowing for separation with a magnet after adsorption is complete and facilitating rapid adsorption and separation of pollutants in wastewater.

1. Introduction

Currently, aromatic pollutants, including dyes and endocrine-disrupting compounds (EDCs), have caused severe environmental pollution and threaten human health.[1,2] Dyes are widely used in the textile, leather, printing, paper, cosmetic, and food industries.[3,4] However, these dye molecules are highly toxic, potentially carcinogenic, and can cause organic mutations or allergies in exposed organisms.[5,6] Bisphenol A (BPA), a common type of EDC, is widely used as an industrial chemical in producing plastics and epoxy resins. It is associated with adverse effects on endocrine disruption, reproduction, neural networks, and cardiovascular and immune systems.[7,8] Due to restrictions on BPA in many countries, bisphenol F (BPF) has emerged as an alternative, but it is also not well controlled in the environment.[9] Given the potential threats posed by dyes and bisphenols to the environment and human health, there is an increasing focus on developing effective strategies to mitigate these risks, including biodegradation,[10,11] physical adsorption,[12,13] and chemical degradation.[14,15] Among these treatment methods, adsorption is the simplest and most cost-effective approach.[16,17]

Supramolecular hydrogel materials have gained increasing attention in environmental protection, particularly for pollutant adsorption and treatment, due to their excellent water content, high porosity, good biocompatibility, and processability.[18–20] Unlike traditional hydrogels, the dynamic, reversible, and weaker nature of noncovalent interactions in supramolecular hydrogels enables them to respond to various external stimuli, including temperature,[21] pH,[22] pressure,[23] light,[24] electric fields,[25] and magnetic fields.[26] For example, magnetically responsive supramolecular hydrogels have excellent application prospects in water treatment. After selectively adsorbing pollutants, it can be easily separated using magnets, thus reducing the cost of wastewater treatment. Furthermore, cyclodextrins (CDs), the well-known natural supramolecular macrocyclic compounds, are a class of cyclic oligosaccharides composed of $_D$-pyranose glucose units linked by α-1,4-glycosidic bonds.[27,28] Currently, CDs and their derivatives are regarded as ideal materials for constructing hydrogel adsorbents.[29] β-CD possesses a hydrophilic exterior and a hydrophobic cavity, allowing it to form host-guest complexes with hydrophobic substances, thereby encapsulating hydrophobic pollutants within the CD cavities.[30,31] Liu et al. successfully constructed a series of negatively charged supramolecular hydrogels consisting of amino-modified β-CD-based polypseudorotaxanes and nanosheets.[32] The hydrogels demonstrated excellent adsorption capacities for cationic dyes, attributed to their porous network structure and the electrostatic

W.-J. An, X.-Y. Yu, C.-H. Liu, Y.-L. Leng, Y. Chen, Y. Liu
College of Chemistry
State Key Laboratory of Elemento-Organic Chemistry
Nankai University
Tianjin 300071, P. R. China
E-mail: chenyong@nankai.edu.cn; yuliu@nankai.edu.cn

The ORCID identification number(s) for the author(s) of this article can be found under https://doi.org/10.1002/adsu.202500018

DOI: 10.1002/adsu.202500018

interactions between the hydrogels and the dyes. Specifically, the adsorption capacity of the hydrogels for Rhodamine B, crystal violet (CV), and methylene blue (MB) could reach 181–228 mg g^{-1}. Peng et al. reported a novel hydrogel composed of cyclodextrin polymer (P-CD) and ferrocene-modified polyacrylic acid, which was associated with the host-guest interaction between P-CD and ferrocene molecules.[33] The adsorption of the hydrogel for BPA was mainly through host-guest interactions, while the adsorption for MB was through hydrogen bonding and electrostatic interactions.

Herein, a magnetic supramolecular hydrogel was prepared by thermal polymerization of acrylamide (AAm), 2-acrylamido-2-methylpropane sulfonic acid (AMPS), acrylated β-CD (β-CDA), and Fe_3O_4 nanoparticles (Fe_3O_4 NPs), following by an assessment of its ability to adsorb pollutants, including CV, MB, BPA, and BPF. The synthesis of pure Fe_3O_4 NPs was verified in transmission electron microscopy (TEM), X-ray diffraction (XRD), and X-ray photoelectron spectroscopy (XPS) experiments. Additionally, the hydrogel was systematically characterized through scanning electron microscopy (SEM), XRD, XPS, and rheological tests. Due to the addition of Fe_3O_4 NPs, the hydrogel can be rapidly collected to one side of the solution under the influence of a magnetic field, facilitating the quick separation of the adsorbent. Moreover, the adsorption kinetic experiments demonstrated that the hydrogel exhibited excellent removal efficacy, with the process of adsorption kinetics described through quasi-first-order, quasi-second-order, and Weber-Morris intraparticle diffusion models to obtain the reaction rate constants (k_n) and the equilibrium adsorption quantities (Q_e). The maximum adsorption capacities (Q_m) were also obtained through adsorption isotherm experiments. Importantly, the hydrogel exhibited excellent removal efficacy in different pH, temperatures, inorganic salt (NaCl) concentrations, humic acid (HA) concentrations, and environmental water samples. Additionally, the regeneration of the hydrogel was successfully achieved, indicating that the hydrogel had significant practical application value. This study is expected to provide a novel strategy for constructing magnetic supramolecular hydrogels as adsorbents that can remove cationic dyes and bisphenols pollutants (**Scheme 1**).

2. Results and Discussion

2.1. Synthesis and Characterization

β-CDA was successfully synthesized through a nucleophilic substitution reaction. By comparing the integral ratios of H-1 protons at 4.9–5.1 ppm to the —CH═CH_2 protons at 5.8-6.5 ppm in the ^1H NMR spectrum, the degree of substitution of β-CDA was determined to be 1.5 (Figure S1, Supporting Information). The spherical Fe_3O_4 NPs, which were modified with sodium citrate and synthesized through a co-precipitation method, exhibited 15–20 nm in diameter in TEM images (**Figure 1a**). The crosslinked Fe_3O_4-P(AAm-AMPS-CDA) hydrogel was constructed by thermally initiated polymerization of AAm, AMPS, β-CDA, Fe_3O_4 NPs, and MBA in the presence of KPS. SEM images of lyophilized hydrogel demonstrated that the hydrogel formed a densely crosslinked network structure (Figure 1b). The Fourier Transform infrared spectroscopy (FTIR) spectrum of β-CDA revealed C = O stretching vibrations corresponding to the ester carbonyl group at 1723 cm^{-1} and a stretching vibration peak representing a carbon-carbon double bond at 1633 cm^{-1}, confirming that a double bond was successfully introduced to β-CD (Figure S2a, Supporting Information). In the FTIR spectrum of Fe_3O_4 NPs, significant absorbance peaks corresponding to the C═O asymmetric stretching, C—O symmetric stretching from the -COOH group of sodium citrate, and Fe-O stretching vibration were observed at 1578, 1386, and 571 cm^{-1}, respectively (Figure S2b, Supporting Information). Additionally, the construction of the hydrogel was confirmed by the peak at 3500-3100, 1673, 1221 cm^{-1} assigned to the basic stretching vibrations of —OH, —NH groups, C═O stretching vibrations, and S═O stretching (Figure S2c, Supporting Information).

Furthermore, the impact of magnetic hydrogel formation on Fe_3O_4 NPs was demonstrated through XRD, XPS, and magnetic hysteresis loops experiments. The XRD analysis of Fe_3O_4 NPs demonstrated characteristic peaks at 2θ = 30.18°, 35.62°, 43.26°, 53.54°, 57.08°, and 62.58°, which corresponded to the diffraction planes of (220), (311), (400), (422), (511), and (440), respectively, thereby confirming the formation of pure Fe_3O_4 NPs. After the formation of the hydrogel, a single broad peak was observed, indicating the disordered structure of the hydrogel (Figure 1c). The valence state of Fe in Fe_3O_4 NPs and hydrogel was verified through XPS testing. The analysis revealed characteristic peaks at binding energies of 710.2 eV and 723.9 eV, corresponding to two different Fe metal states in Fe_3O_4 NPs, namely Fe 2p 3/2 and Fe 2p 1/2 (Figure S3, Supporting Information). Notably, these peaks persisted following the formation of the hydrogel, indicating that the formation of hydrogel would not affect the valence state of Fe. Figure 1f,g illustrated the magnetic separation process of Fe_3O_4 NPs and the hydrogel. In the absence of a magnetic field, Fe_3O_4 NPs were dispersed in water. However, the application of a magnetic field resulted in the rapid aggregation of both Fe_3O_4 NPs and the hydrogel on one side of the field. The magnetic properties of Fe_3O_4 NPs and the hydrogel were also evaluated through magnetic hysteresis loops. The magnetic saturation values of Fe_3O_4 NPs and the hydrogel were 58 emu g^{-1} and 0.4 emu g^{-1}, respectively (Figure 1d,e). The reduction in the magnetic saturation value indicated a shielding effect caused by the incorporation of Fe_3O_4 NPs within the hydrogel. These results demonstrated that the hydrogel exhibited significant magnetic separation capabilities, facilitating rapid and efficient adsorption followed by subsequent recycling.

The mechanical properties of the hydrogel were investigated by rheological tests. In the frequency scanning tests, the storage modulus (G') consistently exceeded the loss modulus (G") as the frequency increased from 0.1 to 100 rad s^{-1}, indicating that the hydrogel maintained a stable state in the situation (**Figure 2a**). In the stress scanning tests, as the stress increased from 0.01% to 5000%, the G' initially surpassed the G" and then tended towards the intersection, indicating the destruction of the hydrogel (Figure 2b). Subsequently, continuous step strain tests were performed to assess the self-healing capabilities of the hydrogel at a constant frequency (1 Hz). At a high strain of 1000%, the G' of the hydrogel decreased, resulting in a transition to a sol-gel state. However, upon reducing the strain to 2%, the hydrogel exhibited a rapid recovery of mechanical strength within 60 s (Figure 2c). These results indicated that the hydrogel had sol-gel

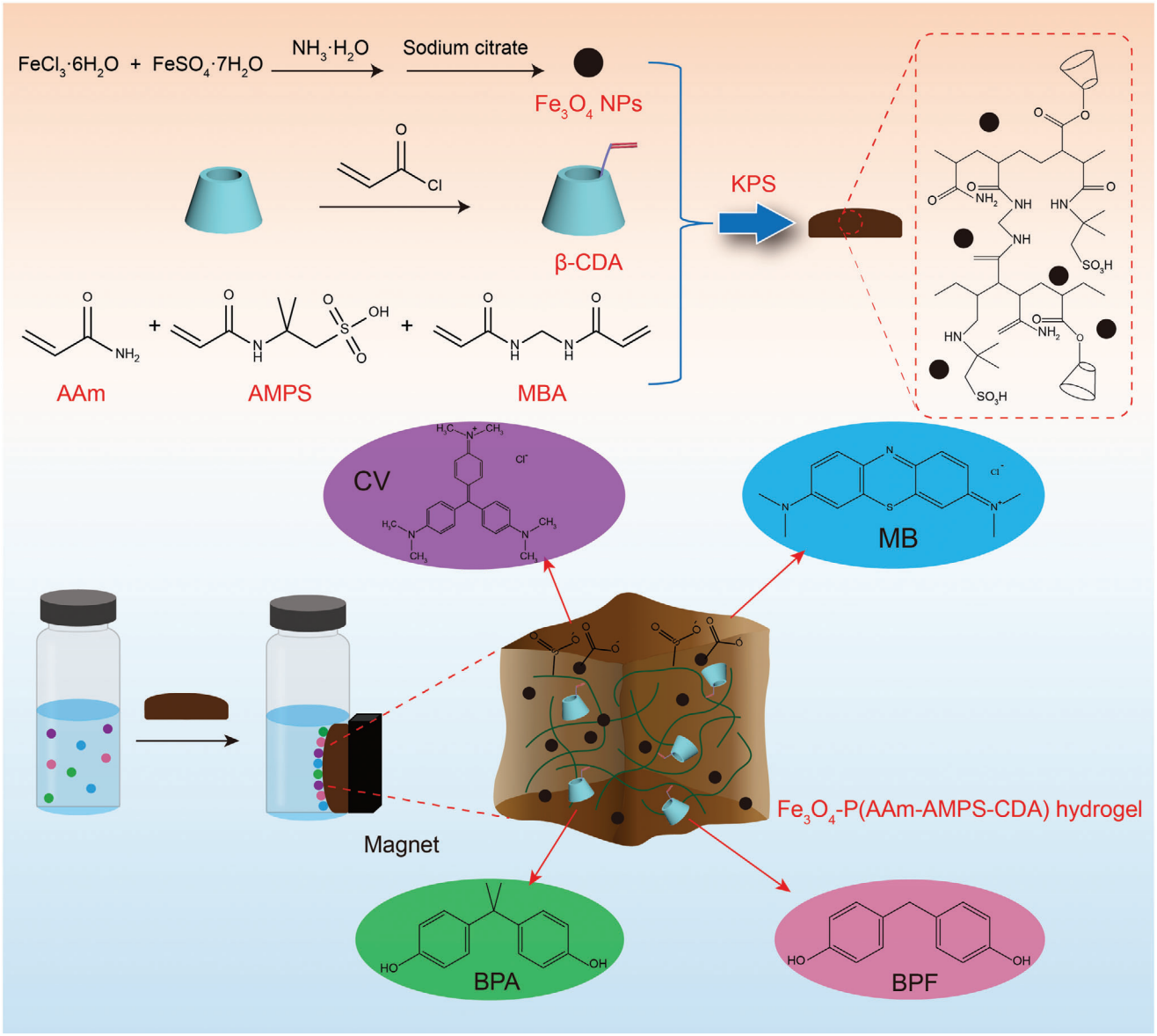

Scheme 1. Construction of Fe_3O_4-P(AAm-AMPS-CDA) hydrogel and the adsorption process for CV, MB, BPA, and BPF.

transformation ability and self-healing properties. The thermogravimetric (TG) analysis was performed to evaluate the composition of Fe_3O_4 NPs and the hydrogel. The mass loss of Fe_3O_4 NPs at 100–450 °C was about 5%, which can be attributed to the thermal degradation influenced by impurities introduced in the co-precipitation preparation process. The mass loss of the hydrogel at 0–250 °C may be attributed to the elimination of water from the hydrogel structure, while the mass loss at 250–450 °C was associated with the breakdown of P(AAm-AMPS-CDA) molecular backbone in the hydrogel. These results indicated that the hydrogel exhibited significant thermal stability below 250 °C (Figure 2d). The zeta potentials of Fe_3O_4 NPs and the hydrogel were -30.5 mV and -35.6 mV, respectively (Figure S4, Supporting Information). The high negative potentials indicated that the hydrogel could adsorb positively charged dyes through electrostatic interactions.

2.2. Adsorption Kinetics Experiment

After characterizing the hydrogel, we further investigated its adsorption capacities for the cationic dyes CV and MB, as well as bisphenols BPA and BPF. In a typical experiment, 100 mg hydrogel was added to 5 mL of 5 mg L^{-1} of CV or MB solution (C_0 = 100 mg L^{-1} for BPA and BPF, solution volume = 5 mL, hydrogel dosage = 150 mg), and then UV–vis spectrum of the solution at different time points was measured after separating the hydrogel with a magnet until adsorption equilibrium was reached (Figure S5, Supporting Information). The adsorption amount and adsorption rate of the hydrogel at different time points can be determined using Equations (1), (2), and the standard curves (Figure S6, Supporting Information) to obtain the adsorption kinetic curves of the hydrogel (**Figure 3**a–d). MB and CV belongs to positively charged organic molecules, thus the hydrogel with high

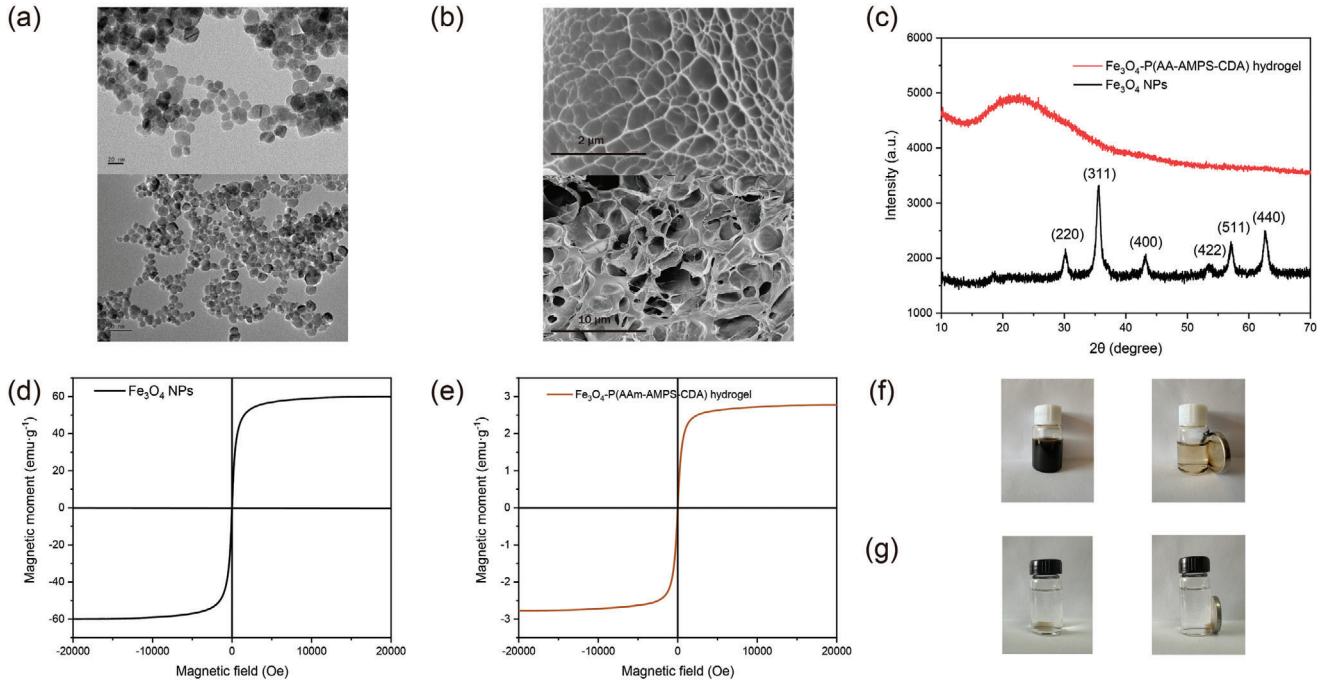

Figure 1. a) TEM images of Fe_3O_4 NPs. b) SEM images of the hydrogel. c) XRD images of Fe_3O_4 NPs and the hydrogel. Magnetic hysteresis loops of d) Fe_3O_4 NPs and e) the hydrogel. Magnetic separation photographs of f) Fe_3O_4 NPs and g) the hydrogel under the influence of a magnetic field.

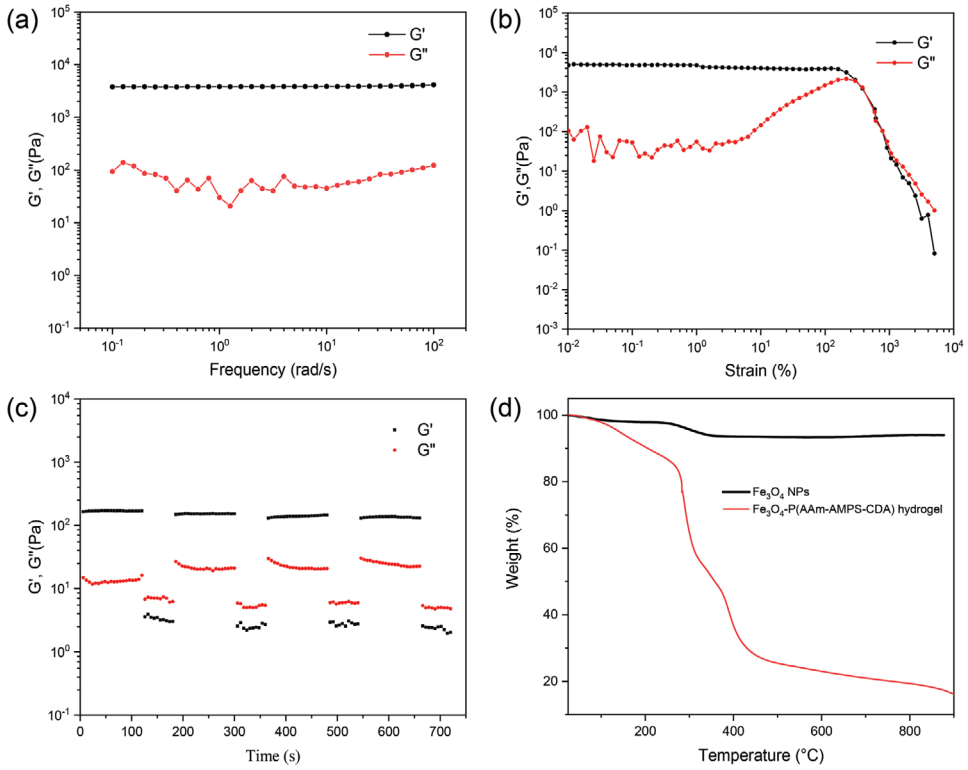

Figure 2. a) Frequency sweep test of the hydrogel at frequency (ω) = 0.1–100 rad s^{-1} and strain (γ) = 2% at 25 °C. b) Strain sweep test of the hydrogel at γ = 0.01-5000% and ω = 1 rad s^{-1}. c) Continuous step strain test of the hydrogel at γ = 2%, 1000%, and ω = 1 Hz. d) The TG curves of Fe_3O_4 NPs and the hydrogel.

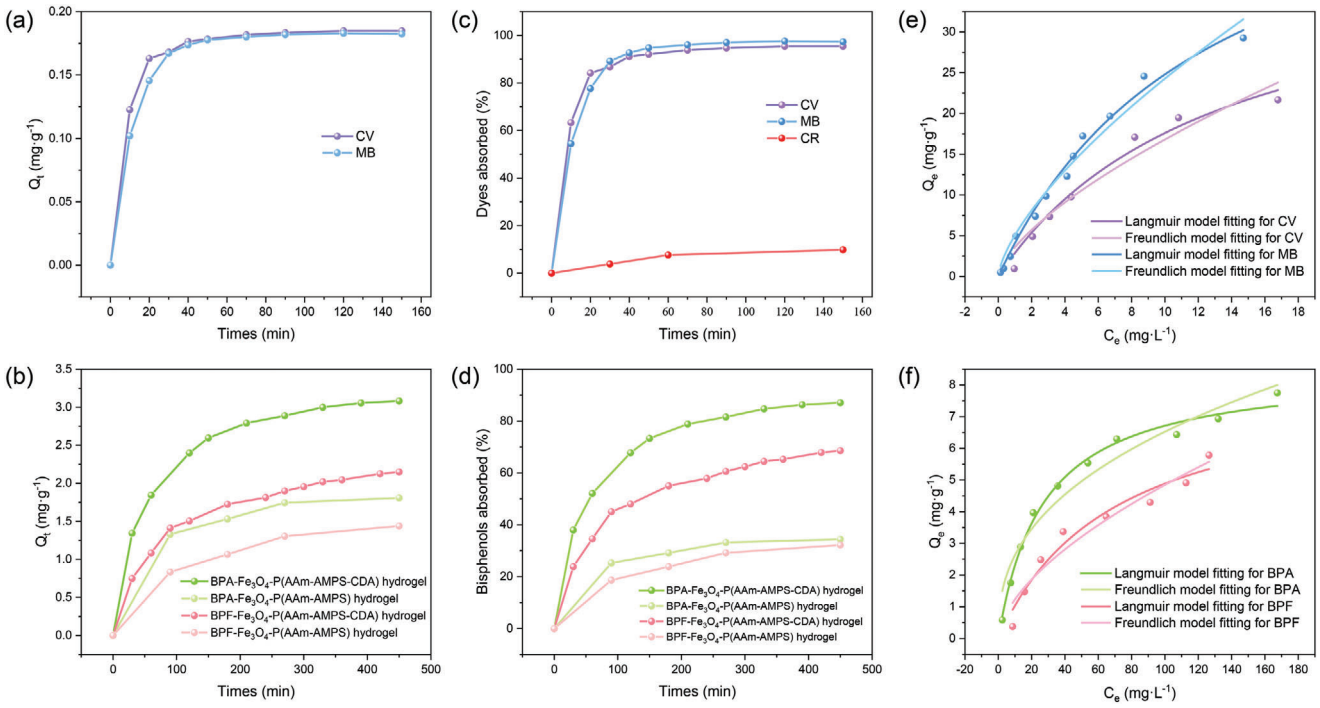

Figure 3. Adsorption kinetics of a) CV, MB (C_0 = 5 mg L^{-1}, solution volume = 5 mL, hydrogel dosage = 100 mg) and b) BPA, BPF (C_0 = 100 mg L^{-1}, solution volume = 5 mL, hydrogel dosage = 150 mg) on the hydrogel. The adsorption rate variation of the hydrogel for c) CV, MB, CR, and d) BPA, BPF over time. Adsorption isotherm of e) CV, MB (C_0 = 10–600 mg L^{-1}, solution volume = 5 mL, hydrogel dosage = 100 mg) and f) BPA, BPF (C_0 = 20–400 mg L^{-1}, solution volume = 5 mL, hydrogel dosage = 150 mg) on the hydrogel and fitted curves with Langmuir and Freundlich model.

negative potentials can trap MB and CV through electrostatic interactions. At the beginning of the adsorption process (0–20 min), the hydrogel exhibited a rapid increase in the adsorption capacity for CV and MB, achieving about 80% of the total adsorption amount. These rapid adsorptions were a consequence of the large pore size of the hydrogel and abundant citrate and sulfonate. Following 100 min of adsorption, the adsorption equilibrium was reached, with the adsorption amounts of the hydrogel for CV and MB at 0.185 and 0.182 mg g^{-1}, respectively (Figure 3a). The decrease in adsorption rates was due to the fact that, as the adsorption time increased, the surface of the hydrogel was gradually occupied by pollutants, leading to a reduction in adsorption sites. The results indicated that the hydrogel could rapidly adsorb CV and MB with adsorption rates of 96% and 98%, respectively, while the adsorption rate for the anionic dye congo red was only 9.84% (Figure 3c). It is well known that bisphenol compounds are hydrophobic small molecules that can enter the cavity of β-CD through hydrophobic interactions to form host-guest inclusion complexes.[31,33] The effect of β-CDA on adsorption was investigated by comparing the adsorption rates of Fe_3O_4-P(AAm-AMPS-CDA) hydrogel and Fe_3O_4-P(AAm-AMPS) hydrogel for BPA and BPF. Similarly, the adsorption of the Fe_3O_4-P(AAm-AMPS-CDA) hydrogel for BPA and BPF could reach about 80% of the total adsorption amount in 120 min, and the adsorption amount and adsorption rates were 3.083 mg g^{-1}, 88%, and 2.149 mg g^{-1}, 69% in 450 min, respectively. However, the adsorption amount and adsorption rates of the Fe_3O_4-P(AAm-AMPS) hydrogel for BPA and BPF were only 1.808 mg g^{-1}, 35%, and 1.438 mg g^{-1}, 32%, respectively (Figure 3b,d). This significant difference demonstrated the critical role of β-CDA cavities in the adsorption of BPA and BPF. Therefore, it is not only hydrogen bonding, including O-H···O and O-H···N, but also the host-guest interactions that play a significant role in the adsorption of BPA and BPF.

$$Q_t = \frac{(C_0 - C_t) \times V}{m} \quad (1)$$

$$Adsorption\ rate\ (\%) = \frac{C_0 - C_t}{C_0} \times 100\% \quad (2)$$

where Q_t (mg g^{-1}) is the adsorption amount at different time points; C_0 and C_t (mg L^{-1}) are the concentrations of dyes and bisphenols before and after absorption; V (L) is the volume of the solution; m (g) is the weight of the hydrogel.

To further study adsorption kinetics, the quasi-first-order, quasi-second-order, and Weber-Morris intraparticle diffusion models were employed to analyze the adsorption data. The pseudo-first-order kinetics describes a linear relationship between adsorption time and the adsorption rate. The pseudo-second-order kinetics model suggests that the adsorption rate is determined by the number of vacancies on the surface of the adsorbent, where chemical adsorption plays an important role. The results of the fitted curves and the kinetic adsorption parameters derived from these models were presented in **Figure** 4a–f and Table S1 (Supporting Information). The calculated k_1 and Q_e ($Q_{e\ (cal)}$) values of the hydrogel for CV and BPA from the quasi-first-order model were 0.020 and 0.0047, and 0.0555 mg g^{-1} and 2.2054 mg g^{-1}, respectively, with correlation

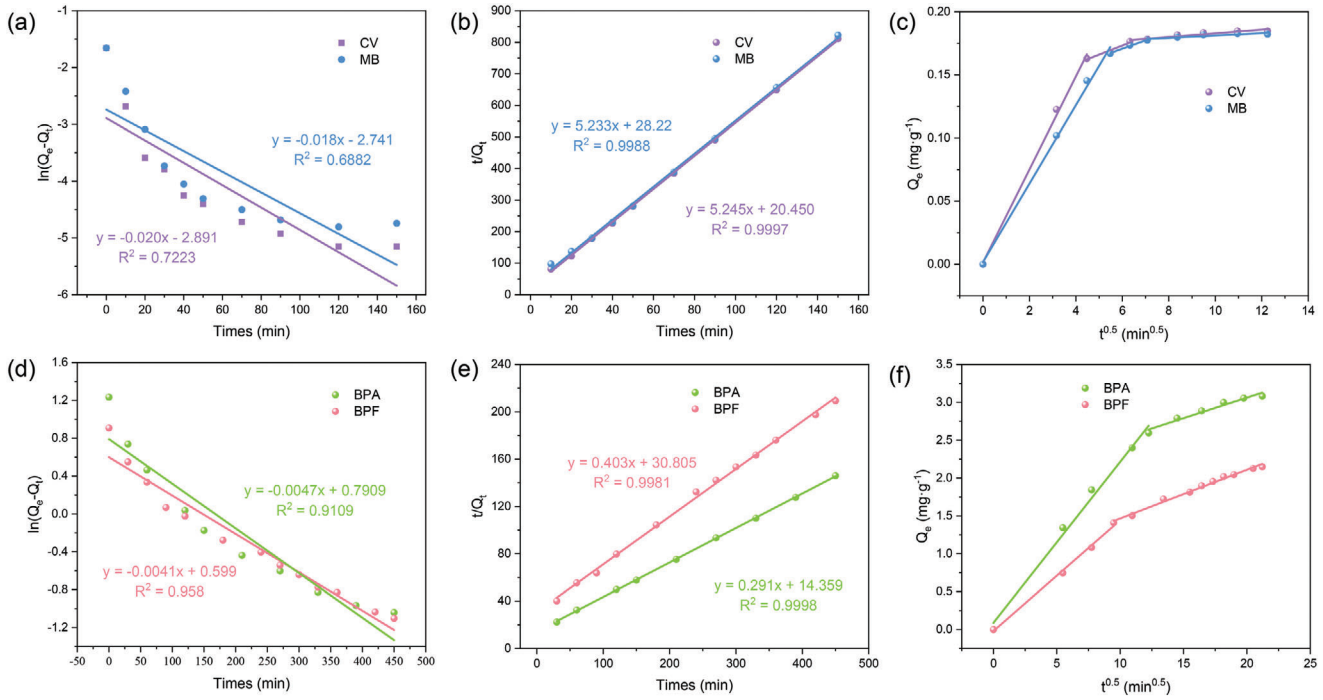

Figure 4. Quasi-first-order kinetics of a) CV, MB, and d) BPA, BPF adsorption on the hydrogel. Quasi-second-order kinetics of b) CV, MB, and e) BPA, BPF adsorption on the hydrogel. Intraparticle diffusion kinetics of c) CV, MB, and f) BPA, BPF adsorption on the hydrogel.

coefficients (R^2) values of 0.7223 and 0.9109. In contrast, the calculated k_2 values from the quasi-second-order kinetic model were 1.345 and 0.0059, $Q_{e\ (cal)}$ values were 0.1907 mg g^{-1} and 3.436 mg g^{-1}, and R^2 values were 0.9997 and 0.9998, respectively. Compared to the quasi-first-order model, the $Q_{e\ (cal)}$ values of the hydrogel for CV and BPA from the quasi-second-order kinetic model were closer to the experimental Q_e ($Q_{e\ (exp)}$) values ($Q_{e\ (exp)}$ value for CV was 0.1849 mg g^{-1}, and $Q_{e\ (exp)}$ value for BPA was 3.0832 mg g^{-1}), and exhibited higher R^2 values. Similar results were also obtained in the hydrogel adsorption of MB and BPF from the adsorption models. Therefore, the adsorption process could be inferred to follow the pseudo-second-order kinetics model, which is due to the fact that the adsorption sites in the hydrogel are gradually occupied as the adsorption time increases, and the gradual decrease of the vacancies on the surface of the adsorbent makes the adsorption rate not linear with the adsorption time. Further, the Weber-Morris intraparticle diffusion model was applied to reveal the diffusion mechanism and predict the control steps in the reaction. The graphs of Q_t versus $t^{0.5}$ are shown in Figure 4c,f, and the corresponding thermodynamic parameters are shown in Table S1 (Supporting Information). Three linear regions were shown in the intraparticle diffusion graphs of the hydrogel for CV and MB, with decreasing internal diffusion rate constants: $k_{d1} > k_{d2} > k_{d3}$. The fastest rate of surface diffusion, represented by k_{d1}, corresponded to the diffusion of the dye through the boundary layer to the surface of the hydrogel. Following the intermediate rate of the intraparticle diffusion process, represented by k_{d2}, corresponds to the transport of CV or MB from the surface of the hydrogel to its interior. The slowest rate of the equilibrium process, represented by k_{d3}, corresponded to the interaction of CV or MB with the active sites of the hydrogel until adsorption equilibrium was reached. The fitting results demonstrated a progressive increase in C_i ($C_1 < C_2 < C_3$), indicating that the diffusion capacity of the hydrogel for CV, MB, BPA, and BPF gradually increased during the adsorption process. The intraparticle diffusion graphs of the hydrogel for BPA and BPF exhibited only two linear regions, with $k_{d1} > k_{d2}$ and $C_1 < C_2$ (Table S1, Supporting Information). This observation was consistent with a fast process of BPA or BPF from the solution to the hydrogel surface, followed by a slower diffusion corresponding to BPA or BPF into the hydrogel structure and β-CDA cavities.

2.3. Adsorption Isotherm Experiment

The adsorption isotherm experiments were performed to demonstrate the correlation between Q_e and equilibrium adsorption concentration (C_e), further estimating the Q_m of the hydrogel for the solution. Data on adsorption isotherms were analyzed and fitted to the Langmuir and Freundlich models (Figure 3e,f and Table S2, Supporting Information). Compared to the Freundlich model (CV: $R^2 = 0.9516$, MB: $R^2 = 0.9744$, BPA: $R^2 = 0.9522$, BPF: $R^2 = 0.9583$), the R^2 values from the Langmuir model showed a stronger correlation (CV: $R^2 = 0.9769$, MB: $R^2 = 0.9904$, BPA: $R^2 = 0.9911$, BPF: $R^2 = 0.9432$). Therefore, the Langmuir model proved to be a better fit for the adsorption process of the hydrogel for CV, MB, BPA, and BPF, indicating that the monolayer adsorption process may occur on a uniform surface. Additionally, the Q_m values of the hydrogel for CV, MB, BPA, and BPF, as determined by the Langmuir isotherm model, were 40.849, 56.534, 8.525, and 8.326 mg g^{-1}, respectively.

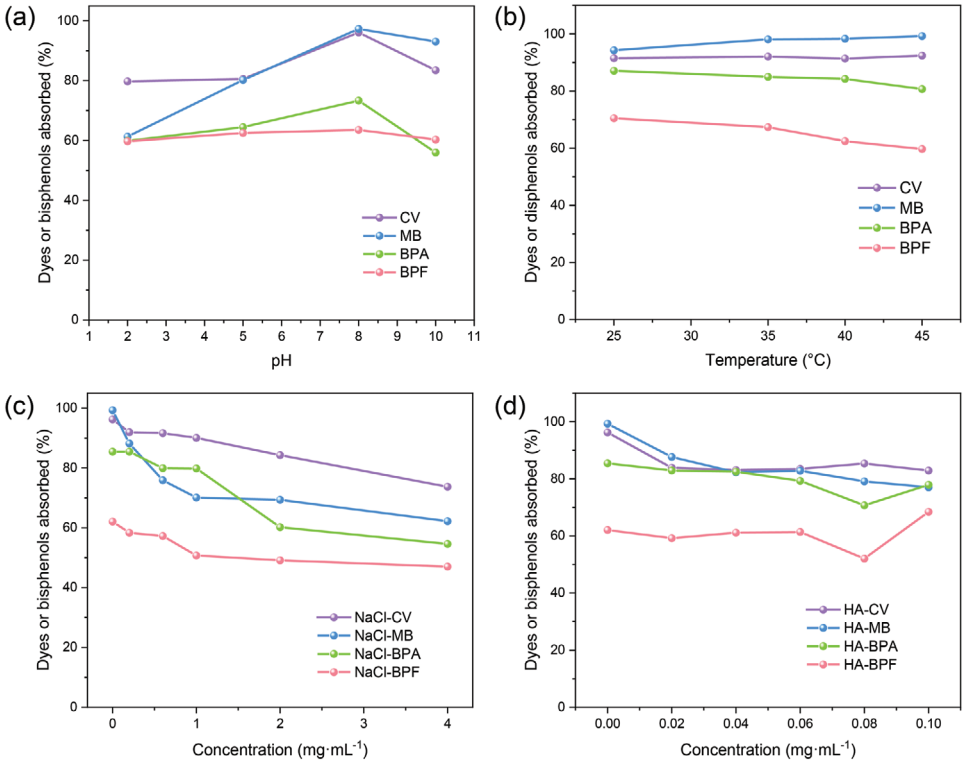

Figure 5. Effect of a) pH and b) temperature (°C) on the adsorption of the hydrogel for CV, MB, BPA, and BPF. Effect of coexisting c) NaCl and d) HA on the adsorption of the hydrogel for CV, MB, BPA, and BPF.

2.4. Effect of Experimental Factors on Adsorption Efficiency

2.4.1. Effect of pH

The pH of an adsorbent is a crucial factor influencing the adsorption rate, as its change affects the form and surface charge of the adsorbent. With the increase in solution pH, the adsorption rates of the hydrogel for CV and MB exhibited a trend of initially increasing and then decreasing (**Figure** 5a). The adsorption rate under alkaline conditions was higher than that under acidic conditions because excess H^+ would compete with CV and MB for adsorption sites, leading to a reduction in adsorption rates. As the pH increased to 8, the increased concentration of OH^- in the solution deprotonated the surface of the hydrogel, thereby enhancing the adsorption of hydrogel for CV and MB. However, when the pH increased from 8 to 10, adsorption became unfavorable, likely due to the formation of hydrogen bonds between OH^- in solution and CV or MB cations, which inhibited the adsorption process. Similarly, as the solution pH increased, the adsorption rates of the hydrogel for BPA and BPF increased and then slightly decreased. When the pH of the solution increased from 2 to 8, the adsorption rate increased, which can be attributed to the electrostatic repulsion within carboxylate groups that caused the expansion of the hydrogel, thereby facilitating the entry of BPA or BPF into the structure of hydrogel and β-CDA cavities. However, when the pH was further increased to 10, BPA and BPF may dissociate into monovalent or divalent anions, which would produce electrostatic repulsion with the negatively charged hydrogel, resulting in a slight decrease in the adsorption rate.

2.4.2. Effect of Temperature

Meanwhile, the effect of temperature on the adsorption rate was further studied. The main adsorption driving force of the hydrogel for CV and MB was electrostatic interactions, which were less affected by temperature. As the temperature increased from 25 °C to 45 °C, the adsorption rate of the hydrogel for CV remained unchanged, while the adsorption rate for MB exhibited a slight increase (Figure 5b). This phenomenon may be attributed to the increased temperature, which accelerated the movement of MB and enhanced the probability of its contact with the adsorbent. Differently, the adsorption rates of the hydrogel for BPA and BPF decreased with increasing temperature. This decline may be because the inclusion of β-CDA and BPA or BPF was exothermic, and the increased temperature was detrimental to the host-guest encapsulation process.

2.4.3. Effect of NaCl and HA

To assess the potential of the hydrogel for application in real water bodies, NaCl and HA were introduced into the solution to study the effect of high concentrations of salt and natural organic matter on the adsorption. With the increase in NaCl concentration from 0.2 to 4 mg mL^{-1}, the adsorption rates of the hydrogel for CV, MB, BPA, and BPF exhibited a decreasing trend. This phenomenon may be attributed to the fact that as the ionic strength increased, Na^+ would cause the shrinkage of some of the pores in the adsorbents, thereby hindering the smooth entry of

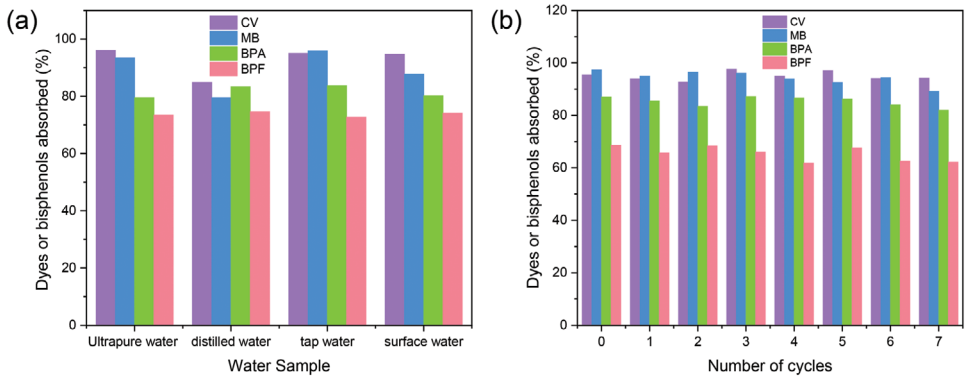

Figure 6. a) Effect of different water samples, including ultrapure water, distilled water, tap water, and surface water, on the adsorption of the hydrogel for CV, MB, BPA, and BPF. b) Effect of adsorption-desorption cycles on the adsorption capacity of the hydrogel for CV, MB, BPA, and BPF (C_0 = 5 mg L^{-1} for CV and MB, solution volume = 5 mL, hydrogel dosage = 100 mg; C_0 = 100 mg L^{-1} for BPA and BPF, solution volume = 5 mL, hydrogel dosage = 150 mg).

pollutants into these pores. In addition, the decrease in the adsorption rates may also be attributed to the fact that Na^+ had a stronger adsorption affinity for COO^- and SO_3^- on the adsorbent, resulting in weakened electrostatic interactions between dyes and the adsorbent (Figure 5c). As the concentration of HA increased from 0.02 to 0.1 mg mL^{-1}, the adsorption rates of the hydrogel for CV and MB decreased, which were attributed to the fact that HA could occupy more adsorption sites and compete with CV and MB for adsorption. Differently, the adsorption rates of the hydrogel for BPA and BPF exhibited a trend of initially decreasing and then increasing. When the concentration of HA increased from 0.02 to 0.08 mg mL^{-1}, HA molecules were long-chained, allowing a portion of the HA structure to be encapsulated in the hydrophobic cavity of β-CDA and to preferentially contact the active sites of the adsorbent (Figure 5d). With the concentration of HA increased to 0.1 mg mL^{-1}, the chains of HA were condensed, leading to the shielding of carboxyl and other functional groups within the molecular structure, resulting in reduced reactivity and adsorption rates. In addition, the hydroxyl, carboxyl, and hydrophobic functional groups of HA could form new complexes with BPA and BPF through hydrogen bonding interactions, which increased the adsorption rates of the hydrogel for BPA and BPF.

2.4.4. Effect of Environmental Matrices

The impact of different environmental matrices on the adsorption rates of the hydrogel was investigated by comparing the adsorption rates for pollutants in ultrapure water, distilled water, tap water, and surface water of Nankai University's Xin Kai Lake. The adsorption rates of the hydrogel for CV and MB in ultrapure water, tap water, and distilled water exhibited relative stability. In contrast, the adsorption rates of the hydrogel for CV and MB in surface water decreased by 10% and 13%, respectively (**Figure 6a**). Interestingly, the hydrogel demonstrated consistently high adsorption rates for BPA and BPF in different environmental matrices, with variations in the adsorption rates controlled within 4% and 2%, respectively. These results suggested that the influence of environmental matrices on the adsorption rates of the hydrogel for CV, MB, BPA, and BPF was minimal, indicating that the hydrogel has significant potential for practical applications as an effective adsorbent for dyes and bisphenols.

2.5. Regeneration and Reusability

The reusability of an adsorbent can significantly reduce the costs associated with industrial production and mitigate the adverse effects of adsorbents on the environment. In this study, the reusability of the hydrogel was investigated through adsorption-desorption experiments. The experimental amount of the hydrogel was introduced into the pollutant solutions, after which the hydrogel was separated by a magnet after achieving the adsorption equilibrium. Subsequently, the hydrogel was immersed in 0.1 M HCl for 12 h to treat CV and MB or in 0.1 M methanol to treat BPA and BPF. The regeneration of the hydrogel was accomplished by immersing it in a 0.1 M NaOH solution for 8 h, followed by washing it with distilled water until it reached a neutral pH for the next cycle. The results demonstrated that the adsorption rates of the hydrogel for CV, MB, BPA, and BPF remained relatively stable after seven adsorption-desorption cycles, with adsorption rates exceeding 93%, 89%, 83%, and 62%, respectively (Figure 6b). SEM experiment showed that the hydrogel still maintained its porous network structure after seven cycles, indicating that regeneration had no effect on the porous structure (Figure S7, Supporting Information). Meanwhile, XPS experiment showed that the various elements in the magnetic hydrogel were consistent with the original hydrogel, and there was no charge in the valence state of iron, indicating that the basic structure of the hydrogel was not affected by regeneration, and that the hydrogel still maintained its magnetic properties (Figure S8, Supporting Information). These results indicated that the hydrogel was a promising adsorbent for the adsorption of cationic dyes and bisphenols.

3. Conclusion

In summary, a magnetic Fe_3O_4-(AAm-AMPS-CDA) supramolecular hydrogel was successfully constructed as an effective

pollutant adsorbent. The adsorption of the hydrogel for CV and MB was achieved through electrostatic interactions, while the adsorption for BPA and BPF was achieved through host-guest interactions and hydrogen bonds. The adsorption kinetic results indicated that the quasi-second-order model provided a more accurate fit for the kinetic data of the four pollutants compared to the quasi-first-order model, and the Weber-Morris intraparticle diffusion model enhanced comprehension of the adsorption process. Additionally, the adsorption isotherm experiment demonstrated that the Langmuir model was more suitable for characterizing the adsorption process of the hydrogel for four pollutants, suggesting that a monolayer adsorption process may occur on a uniform surface. Furthermore, the hydrogel also exhibited effective adsorption rates in the presence of NaCl and HA, as well as under different environmental water quality conditions. More importantly, the hydrogel had magnetic properties, enabling rapid separation from the solution using a magnet. The regenerated hydrogel could be reused for at least seven cycles. All results indicated that the Fe_3O_4-P(AAm-AMPS-CDA) hydrogel is a promising adsorbent for the removal of cationic dyes and bisphenols in the field of pollutant treatment.

4. Experimental Section

Materials: $FeCl_3{\cdot}6H_2O$, $FeSO_4{\cdot}7H_2O$, MB, CV, CR and BPF were purchased from Shanghai Macklin Biochemical Technology Co., Ltd. Sodium Citrate, AMPS, MBA, KPS, β-CD, acryloyl chloride and BPA were purchased from Tianjin Xiensi Biochemical Technology Co., Ltd. AAm, triethylamine and ammonia were provided by Shanghai Aladdin Bio-Chem Technology Co., Ltd. Dimethylformamide, acetone and methanol were purchased from Tianjin Bo Chemical Reagent Co., Ltd.

Instrumentation: The ^{1}H NMR spectra was investigated on a Bruker AV400 spectrometer. The FTIRwas recorded on TENSOR II Fourier transform infrared spectrometer. TEMmeasurements were performed on a high-resolution TEM (Tecnai G2 F20 microscope, FEI) equipped with a CCD camera (Orius 832, Gatan). SEMmeasurements were performed on a JSM-7500F SEM. The zeta potential was measured using the Malvern Panalytical Zetasizer Nano ZS. XPS measurements were performed using an Axis Ultra DLD XPS. TG measurements were performed using a Netzsch STA 409 PC Luxx simultaneous thermal analyzer. Samples were heated at 10 °C min^{-1} from 25 °C to 900 °C in a dynamic nitrogen atmosphere. UV-vis spectra were measured using a Shimadzu UV-3600 spectrophotometer (light path 10 mm, quartz cell).

Preparation of Fe_3O_4 NPs: $FeSO_4{\cdot}7H_2O$ (1.112 g) and $FeCl_3{\cdot}6H_2O$ (2.16 g) were dissolved in H_2O (200 mL), stirred under N_2 atmosphere and heated to 80 °C. Then $NH_3{\cdot}H_2O$ (12 mL) was added to the reaction solution and stirred for 20 min to precipitate the particles. Then, the reaction flask was cooled to room temperature and centrifuged, washed twice with distilled water, and vacuum-dried at room temperature for 18 h. The obtained Fe_3O_4 (2 g) was dispersed into 100 mL of 0.1 mol L^{-1} sodium citrate solution and ultrasonicated under N_2 atmosphere for 30 min. Then, it was transferred to a water bath at 60 °C and stirred for 12 h. After washing with acetone and water, the product Fe_3O_4 NPs were obtained through magnetic separation followed by vacuum drying.

Preparation of β-CDA: β-CD (5 g) was dissolved in DMF (50 mL) and sonicated until the solution was clear, after which a certain amount of triethylamine was added as an acid-binding agent. Then, an appropriate amount of acryloyl chloride (β-CD: acryloyl chloride = 1:8) was dissolved in DMF (5 mL) and then slowly added dropwise into the β-CD solution in an ice water bath under an N_2 atmosphere. After the dropwise addition, the reaction was carried out for 30 min in an ice water bath and then transferred to room temperature for 1 h. At the end of the reaction, the triethylamine hydrochloride was removed by filtration and precipitated by cold acetone. After two filtrations and washes, the β-CDA was obtained through vacuum drying at 40 °C for 12 h. The product β-CDA was obtained from the reaction.

Supporting Information

Supporting Information is available from the Wiley Online Library or from the author.

Acknowledgements

The authors thank the National Natural Science Foundation of China (NNSFC, Nos. 22131008), Fundamental Research Funds for the Central Universities (Nankai University), and the Haihe Laboratory of Sustainable Chemical Transformations for financial support.

Conflict of Interest

The authors declare no conflict of interest.

Data Availability Statement

The data that support the findings of this study are available from the corresponding author upon reasonable request.

Keywords

adsorption, bisphenols, cyclodextrin, dyes, magnetic supramolecular hydrogel

Received: January 6, 2025
Revised: February 14, 2025
Published online:

[1] Y. Han, H. Dai, X. Rong, H. Jiang, Y. Xue, *Molecules* **2023**, *28*, 8028.
[2] D. Biswakarma, N. Dey, S. Bhattacharya, *Langmuir* **2023**, *39*, 11610.
[3] A. Azari, R. Nabizadeh, S. Nasseri, A. H. Mahvi, A. R. Mesdaghinia, *Chemosphere* **2020**, *250*, 126238.
[4] J. Wang, Y. Chen, N. Cheng, L. Feng, B.-H. Gu, Y. Liu, *ACS Appl. Bio. Mater.* **2019**, *2*, 5898.
[5] W. Zhang, Y.-M. Zhang, Y. Liu, *Chem Asian J* **2021**, *16*, 2321.
[6] S. Agnihotri, R. Singhal, *J. Polym. Environ.* **2018**, *26*, 383.
[7] Q. Li, F. Pan, W. Li, D. Li, H. Xu, D. Xia, A. Li, *Polymers* **2018**, *10*, 1136.
[8] W. Cho, D. Lee, G. Choi, J. Kim, A. E. Kojo, C. Park, *Adv. Mater.* **2022**, *34*, 2206982.
[9] T. Wang, L. Xue, L. Zheng, S. Bao, Y. Liu, T. Fang, B. Xing, *J. Hazard. Mater.* **2021**, *416*, 126126.
[10] X. Chen, Y. Dai, M. Zhao, F. E. Löffler, J. Zhuang, *Environ. Sci. Technol.* **2022**, *56*, 11409.
[11] K. Jumnong, P. Kongseng, P. Maijan, S. Suwanboon, S. Chantarak, *Int. J. Biol. Macromol.* **2023**, *253*, 127533.
[12] Y. Dang, Y. Cheng, Y. Zhou, Y. Huang, K. Wang, *Catalysts* **2021**, *11*, 10.
[13] J. Li, C. Fu, M. Zhu, X. Huang, S. Song, F. Dong, *Environ. Pollut.* **2024**, *348*, 123862.
[14] X. He, X. Yang, C. Zhang, Y. Xiao, Y. Tang, *J. Clean Prod.* **2023**, *414*, 137571.
[15] Z.-Q. Liu, L.-Y. Kong, B.-L. Fei, *Appl. Organomet. Chem.* **2024**, *38*, e7599.

[16] V. Rizzi, F. Fiorini, G. Lamanna, J. Gubitosa, E. A. Prasetyanto, P. Fini, F. Fanelli, A. Nacci, L. DeCola, P. Cosma, *Adv. Sustainable Syst.* **2018**, *2*, 1700146.
[17] W. Shang, X. Wang, X. Zhang, C. Zhang, X. Huang, K. Li, *Adv. Sustainable Syst.* **2023**, *7*, 2300164.
[18] Z. Chen, X. Song, W. W. M. Soh, Y. Wen, J. Zhu, M. Zhang, J. Li, *Gels* **2021**, *7*, 201.
[19] R. Wei, W. Song, F. Yang, J. Zhou, M. Zhang, X. Zhang, W. Zhao, C. Zhao, *Ind. Eng. Chem. Res.* **2018**, *57*, 8209.
[20] A. Zhou, W. Chen, L. Liao, P. Xie, T. C. Zhang, X. Wu, X. Feng, *Total Environ.* **2019**, *671*, 377.
[21] S. Xian, M. J. Webber, *J. Mater. Chem. B* **2020**, *8*, 9197.
[22] F. Olate-Moya, H. Palza, *J. Appl. Polym. Sci.* **2022**, *139*, e51420.
[23] Y. Si, L. Wang, X. Wang, N. Tang, J. Yu, B. Ding, *Adv. Mater.* **2017**, *29*, 1700339.
[24] M. S. de Luna, V. Marturano, M. Manganelli, C. Santillo, V. Ambrogi, G. Filippone, P. Cerruti, *J. Colloid Interface Sci.* **2020**, *568*, 16.
[25] B. Xue, M. Qin, T. Wang, J. Wu, D. Luo, Q. Jiang, Y. Li, Y. Cao, W. Wang, *Adv. Funct. Mater.* **2016**, *26*, 9053.
[26] C. Gila-Vichez, L. Rodriguez-Arco, M. C. Mañas-Torres, L. Álvarez de Cienfuegos, M. T. Lopez-Lopez, *Colloid Interface Sci.* **2022**, *62*, 101644.
[27] Z. Liu, Y. Liu, *Chem. Soc. Rev.* **2022**, *51*, 4786.
[28] X. Yu, W. An, L. Jiang, W. Xu, Z. Qian, L. Hua, Y. Chen, Y. Liu, *ACS Appl. Mater. Interfaces* **2024**, *16*, 68229.
[29] R. Zhao, Y. Wang, X. Li, B. Sun, C. Wang, *ACS Appl. Mater. Interfaces* **2015**, *7*, 26649.
[30] N. Hou, R. Wang, R. Geng, F. Wang, T. Jiao, L. Zhang, J. Zhou, Z. Bai, Q. Peng, *Soft Matter* **2019**, *15*, 6097.
[31] Z. Yuan, H. Liu, H. Wu, Y. Wang, Q. Liu, Y. Wang, S. F. Lincoln, X. Guo, J. Wang, *J. Chem. Eng. Data* **2020**, *65*, 678.
[32] Y. Zhang, L. Liang, Y. Chen, X.-M. Chen, Y. Liu, *Soft Matter* **2019**, *15*, 73.
[33] N. Hou, R. Wang, F. Wang, J. Bai, T. Jiao, Z. Bai, L. Zhang, J. Zhou, Q. Peng, *Colloid Surf. A-Physicochem. Eng. Asp.* **2019**, *579*, 123670.